BIOPHYSICS

Isotropic three-dimensional dual-color super-resolution microscopy with metal-induced energy transfer

Jan Christoph Thiele[1], Marvin Jungblut[2], Dominic A. Helmerich[2], Roman Tsukanov[1], Anna Chizhik[1], Alexey I. Chizhik[1], Martin J. Schnermann[3], Markus Sauer[2], Oleksii Nevskyi[1]*, Jörg Enderlein[1,4]*

Over the past two decades, super-resolution microscopy has seen a tremendous development in speed and resolution, but for most of its methods, there exists a remarkable gap between lateral and axial resolution, which is by a factor of 2 to 3 worse. One recently developed method to close this gap is metal-induced energy transfer (MIET) imaging, which achieves an axial resolution down to nanometers. It exploits the distance-dependent quenching of fluorescence when a fluorescent molecule is brought close to a metal surface. In the present manuscript, we combine the extreme axial resolution of MIET imaging with the extraordinary lateral resolution of single-molecule localization microscopy, in particular with direct stochastic optical reconstruction microscopy (*d*STORM). This combination allows us to achieve isotropic three-dimensional super-resolution imaging of subcellular structures. Moreover, we used spectral demixing for implementing dual-color MIET-*d*STORM that allows us to image and colocalize, in three dimensions, two different cellular structures simultaneously.

INTRODUCTION

Super-resolution microscopy has revolutionized optical imaging by extending the limits of spatial resolution by three orders of magnitude down to a few nanometers. The first truly super-resolving microscopy methods were stimulated emission depletion (STED) microscopy (*1*) and later reversible saturable optical fluorescence transitions developed by Hell and co-workers (*2*). This pioneering work spurred the development of another class of super-resolution methods, single-molecule localization microscopy (SMLM), which is based on the idea that one can localize the center position of an individual fluorescent molecule with much higher accuracy than the width of the molecule's image (defined by the optical resolution of a microscope). SMLM comprises methods such as stochastic optical reconstruction microscopy (STORM) (*3*), photoactivatable localization microscopy (PALM) (*4*), point accumulation for imaging in nanoscale topography (PAINT) (*5*) microscopy, its commonly used variant DNA-PAINT (*6*), or direct STORM (*d*STORM) (*7*).

All of the abovementioned methods provide superb lateral resolution, but cellular structures are of course intrinsically three-dimensional (3D). Thus, several approaches have been developed to extend the super-resolution capabilities to the third dimension. For STED, the use of special phase plates allows for generating stimulated emission intensity distributions with particular resolution enhancement along the optical axis (*8*). For SMLM, different techniques have been introduced such as biplane imaging (*9*), astigmatic imaging (*10*), or various point spread function (PSF) designs such as double-helix PSF (*11*), corkscrew PSF (*12*), or tetrapod PSF (*13*). Recently, clever PSF phase self-modulation has been used for 3D SMLM deep in tissue (*14*). However, all these techniques provide an axial resolution that is by a factor of 2 to 3 worse than the achievable lateral resolution (*15*), very similar to the resolution ratios achieved in conventional, diffraction-limited confocal laser scanning microscopy (CLSM).

This gap between lateral and axial resolution was closed by 4π interferometric microscopy techniques that interfere the emission of a molecule detected from two opposite sides two objectives. This leads to a marked improvement in axial resolution as demonstrated by interferometric PALM (*16*), isoSTED (*17*), or whole-cell 4Pi single-molecule switching nanoscopy (*18*). However, these methods are based on macroscopic interferometers that are experimentally very challenging to operate, which prevented their wide distribution and application so far. One of the latest additions to the zoo of 3D SMLM is 3D-MINFLUX (*19*). With 3D-MINFLUX, it is possible to localize single molecules with subnanometer accuracy by detecting as few as some hundred photons (*20*). Moreover, the recently introduced pulsed interleaved MINFLUX simplifies the experimental setup, making it potentially more amenable for wider use (*21*). However, the currently existing versions of MINFLUX suffer from low throughput (number of localized molecules per time) and are still technically more complex than almost all SMLM methods that are based on conventional wide-field microscopes.

An attractive alternative to the abovementioned interferometric methods are techniques based on evanescent fields. The first of these approaches uses the exponentially decaying excitation intensity in a total internal reflection fluorescence microscope (TIRFM), where the sample is illuminated from the glass side with a plane wave incident under a high angle above the critical TIR angle. This illumination generates an evanescent electromagnetic field on the sample side, so that the excitation intensity that a molecule sees depends on its distance from the surface. By taking several snapshots for excitations under different excitation angles and thus modulating the exponential decay of the evanescent field intensity, it is possible to calculate distances of molecules (fluorescent structures) from the surface with a few-nanometer precision (variable-angle TIRFM) (*22*, *23*). Alternatively, one can use the evanescent field of fluorescence emission for measuring molecule-surface distance values. One of the first

[1]Third Institute of Physics–Biophysics, Georg August University, 37077 Göttingen, Germany. [2]Department of Biotechnology and Biophysics, Biocenter, University of Würzburg, Am Hubland, 97074 Würzburg, Germany. [3]Chemical Biology Laboratory, Center for Cancer Research, National Cancer Institute, Frederick, MD 21702, USA. [4]Cluster of Excellence "Multiscale Bioimaging: From Molecular Machines to Networks of Excitable Cells" (MBExC), Georg August University, Göttingen, Germany.
*Corresponding author. Email: oleksii.nevskyi@phys.uni-goettingen.de (O.N.); jenderl@gwdg.de (J.E.)

realizations of this idea was super critical angle fluorescence detection, which uses the fact that the evanescent field of an emitting molecule can couple into propagating light modes on the glass side, which can then be detected with an objective of sufficiently high numerical aperture (NA). This coupling efficiency is again highly distance dependent because of the evanescent nature of the coupled field. By comparing the intensity of this supercritical emission (named so for its emission angles above the critical TIR angle) with "classical" emission below the critical TIR angle (which does not depend on molecule-surface distance), one can again deduce distance values of single molecules with an accuracy of few nanometers (*24*–*26*).

Another technique that exploits the evanescent field of fluorescence emission is metal-induced energy transfer (MIET) (*27*). The technique uses the distance-dependent coupling of the evanescent field of a fluorescent emitter to surface plasmons in a thin metallic layer deposited on the surface of the glass cover slide. The resulting energy transfer is extremely distance dependent and leads to a distance-dependent fluorescence lifetime and intensity of the emitter, which can be used to determine molecule-distance values with nanometer accuracy (single-molecule MIET or smMIET) (*28*–*30*), despite the unavoidable fluorescence intensity losses due to partial light absorption by the metal film. This is due to the fact that, although the fluorescence brightness of a dye is increasingly reduced the closer the dye comes to the metal surface, its photostability increases proportionally, so that the average number of detectable photons from one molecule until photobleaching is nearly independent on dye-metal distance. However, a dielectric nanocoating can substantially improve SMLM performance and increase the lateral localization precision by up to a factor of 2 (*31*). Because of the broad absorption spectra of metals, the energy transfer from a fluorescent molecule to the metal takes place with high efficiency across the full emission spectrum of a molecule. Meanwhile, MIET imaging was successfully used for studying various biological questions, for example, blood platelet spreading and adhesion (*32*), the reorganization of the actin cytoskeleton during epithelial-to-mesenchymal cell transformation (*33*), or the measurement of the interbilayer distance of a nuclear envelope (*34*). An interesting alternative to a metal film as energy acceptor is graphene, which shows a much steeper lifetime-versus-distance dependence (*35*) and allows for achieving an order-of-magnitude better axial localization accuracy down to a few angstroms (*36*–*38*).

Thus, a combination of MIET imaging with the high lateral resolution of SMLM could provide isotropic 3D super-resolution imaging of cellular structures. However, SMLM techniques are traditionally camera based, while MIET relies on precise single-molecule lifetime measurements. To implement fluorescence lifetime–resolved SMLM (FL-SMLM), we have recently combined rapid confocal laser scanning, pulsed excitation, and time-correlated single-photon counting (TCSPC) with SMLM based on *d*STORM or DNA-PAINT (*39*). Although the single molecules are localized exactly as in wide-field SMLM, this technique has several advantages, like a light exposure limited to only the scanned area and optical sectioning that allows imaging deeply into the cell. Most importantly, the TCSPC detection gives access to the fluorescence decay curves of each localization that provides lifetime information on a single-molecule basis. This enables lifetime-based multiplexing within the same spectral window and therefore allows for chromatic aberration-free super-resolution imaging of multiple cellular structures in parallel.

In this work, we present a combination of smMIET with *d*STORM, one of the most powerful and widely used SMLM techniques. Our approach combines all the advantages of FL-SMLM with the exquisite axial resolution of MIET imaging. First, we demonstrate MIET-*d*STORM on surface-immobilized double-stranded DNA (dsDNA) constructs. To show that MIET-*d*STORM can be used for a wide range of biological applications, we imaged microtubules and clathrin-coated pits in fixed U2OS cells. Moreover, dual-color MIET allowed for simultaneous imaging of both structures when using spectral demixing *d*STORM (sd-*d*STORM) (*40*).

RESULTS

Validation of MIET-SMLM

In MIET-SMLM, the axial information is encoded in the fluorescence lifetime. To access the single-molecule lifetimes, we performed FL-SMLM with a custom-built confocal microscope with a fast laser scanner, single-photon detection, and TCSPC electronics (for more details, see fig. S1).

For validation of the method, and to check the axial precision of smMIET, we immobilized Alexa Fluor 647 (AF 647)–dsDNA–biotin constructs on a gold-coated cover glass topped with a SiO_2 spacer layer of well-defined thickness. We used the dye AF 647 for labeling, which is known for its good performance in *d*STORM measurements. Measured TCSPC curves (Fig. 1A) and single-molecule lifetime histograms (Fig. 1B) show the expected lifetime increase with increasing spacer thickness. From the MIET measurements, we deduce that the bovine serum albumin (BSA)–neutravidin immobilization layer has a thickness of ~12 nm, which is in excellent agreement with literature values (*41*). The width of the height distributions (Fig. 1D) reflects the surface roughness and axial localization precision. Therefore, the data confirm that the axial localization precision is below 10 nm up to a height of 60 nm.

Imaging biological structures using MIET-SMLM

3D imaging with MIET-SMLM is compatible with biological samples. To demonstrate this, we seeded cells on a cover glass coated with 10 nm of gold and 5 nm of SiO_2 using standard immunofluorescence sample preparation procedures (see Materials and Methods for details). The SiO_2 layer is crucial to protect the gold from the chemically reductive environment during sample preparation and from the thiols in the imaging buffer. First, we imaged α-tubulin in U2OS cells (see Fig. 2A), which were chosen because of their planarity. The diffraction-limited fluorescence lifetime imaging microscopy (FLIM) image (Fig. 2B) already reveals clear lifetime differences along the microtubules, but the finer details become only visible in the FL-SMLM reconstruction. For each single molecule, lifetime values were converted to height values to obtain its 3D position. In the super-resolved reconstruction from 3D localizations shown in Fig. 2C, subtle height differences on the order of a microtubule diameter become visible in the network. MIET-SMLM does not compromise the lateral localization precision, which we estimated to be 9.1 nm using a modified Mortensen equation (*42*, *43*).

Using MIET does not restrict the choice of possible fluorophores. We have performed MIET-SMLM with several types of fluorophores, such as AF 647 and CF 680 for classical *d*STORM imaging and Cy5b for reductive caging SMLM (see fig. S2) (*44*). For correctly modeling MIET imaging as required for data evaluation (conversion of lifetime into distance values), exact knowledge of emission

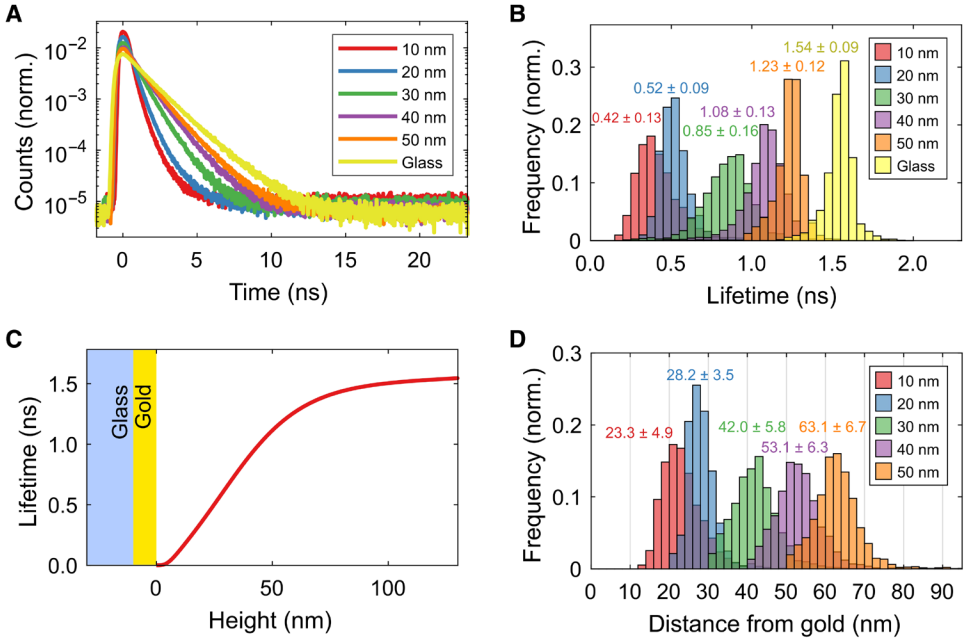

Fig. 1. MIET-SMLM validation. (**A**) TCSPC curves for DNA labeled with AF 647 on MIET substrates with different SiO_2 spacers and on pure glass. (**B**) Single-molecule lifetime histograms of DNA labeled with AF 647 on MIET substrates with different SiO_2 spacers and on pure glass. The lifetime histograms include data from several regions of interest. (**C**) MIET curve for AF 647 above a MIET substrate with a 10-nm gold layer. (**D**) Histograms of axial positions (height values) of single molecules calculated with the MIET curve from their measured lifetimes. Averages and SDs of lifetime and height values are given next to each peak.

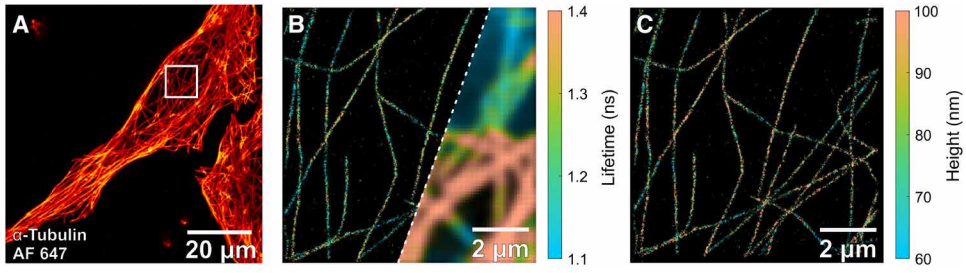

Fig. 2. MIET-*d*STORM imaging in cells. (**A**) Confocal laser scanning image of microtubules in U2OS cells labeled with AF 647. (**B**) Confocal FLIM and super-resolved FLIM image of the region of interest marked in (A). (**C**) Super-resolved height image of the corresponding region of interest.

spectra, fluorescence quantum yields, and fluorescence lifetimes of the used fluorophores (in the absence of any metal quenching) is required. Therefore, we performed lifetime reference measurements on fluorophores far away from the gold-coated cover glass and determined absolute values of fluorescence quantum yield of antibody-conjugated fluorophores using a recently developed nanocavity method (see table S1) (*45*).

Simultaneous dual-color MIET-SMLM

The nature of excitation and detection in a CLSM facilitates extension to spectrally resolved imaging. We implemented dual-color detection by splitting the fluorescence signal, with an additional dichroic mirror, into two separate detection channels, each equipped with a single-photon–sensitive detector (for details, see Materials and Methods and fig. S1). With this system, we performed sd-*d*STORM on U2OS cells with AF 647–labeled α-tubulin and CF 680–labeled clathrin. The spectral and photophysical properties of these two fluorophores make them good candidates for spectral demixing (see fig. S3). In the spectral-resolved reconstruction shown in Fig. 3B, it is straightforward to distinguish the two targets α-tubulin and clathrin. The different relative intensities of the two dyes in the two detection channels allow for classification of single molecules with negligible cross-talk and separate reconstruction of the two targets (fig. S4, A and B). Spectral-splitting CLSM has the advantage that no channel registration is required and that, due to single-photon counting with almost zero dark counts, the signal-to-noise ratio is excellent. Both aspects are important for achieving highest lateral localization precision, which was estimated to be approximately 9.0 nm for both targets (see fig. S4C). Moreover, the spectral splitting does not interfere with the lifetime measurement. Measured lifetime values of AF 647 and CF 680 were converted to height values using the corresponding MIET curve for each fluorophore. In

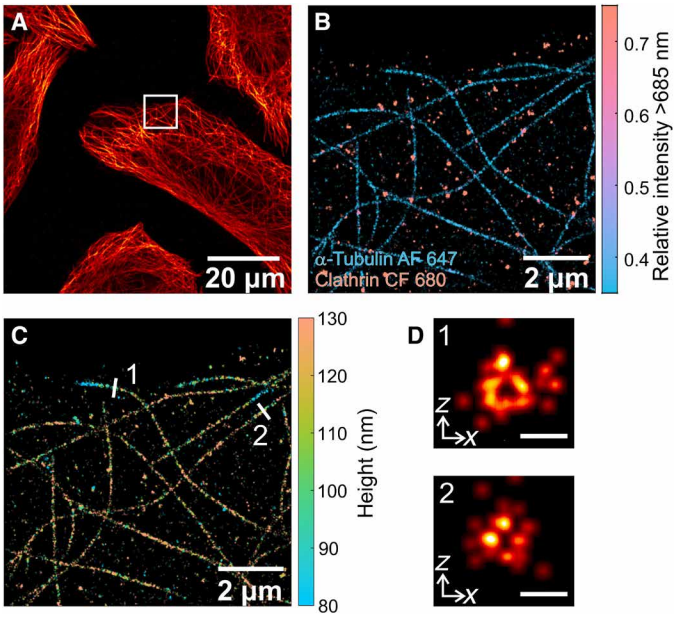

Fig. 3. Simultaneous dual-color MIET-*d*STORM imaging in cells. (**A**) Diffraction-limited confocal laser scanning image of α-tubulin and clathrin in U2OS cells labeled with AF 647 and CF 680, respectively. (**B**) sd-*d*STORM image of the region of interest marked in (A). (**C**) 3D MIET-*d*STORM image of the region of interest marked in (A), where lifetime values were converted to height values and both targets are shown together. (**D**) *xz* cross sections of microtubules 1 and 2 shown in (A). Scale bars, 50 nm.

Fig. 3C, a 3D-*d*STORM image of both targets is presented. Separate super-resolved height images for α-tubulin and clathrin are shown in fig. S4.

DISCUSSION

In this work, we demonstrated that precise axial localization in SMLM can be realized on the basis of the fluorescence lifetime with MIET-SMLM. We validated the high axial accuracy by imaging immobilized dye-dsDNA constructs. To prove that MIET-SMLM is compatible with biological samples, we imaged microtubules in fixed U2OS cells, because they are an established benchmark sample due to their well-defined structure. Additional measurements with various fluorophores confirmed that MIET-SMLM is completely independent of the switching mechanism or measurement conditions.

By integrating spectral demixing, we implemented dual-color MIET-*d*STORM and imaged clathrin and microtubles simultaneously. For both targets, we find structures at height values from below 80 nm to above 130 nm. Clathrin structures are present at different heights, where it is plausible that the lowest structures correspond to forming clathrin-coated pits, while the higher structures might be detached clathrin-coated vesicles. Microtubules can be located at different heights where small sections approach the surface closer than 80 nm. As an example, a corresponding microtubule profile is presented in fig. S4D. To highlight the quality of the obtained 3D data, we plotted *xz* cross sections of the microtubules marked in Fig. 3D. The hollow structure and the size of the microtubules match theoretical expectations when taking into account that the labeling with secondary antibodies adds an additional distance between the fluorophores and the imaged structures (*46*). Our data confirm that MIET-STORM archives high localization precision in all 3D in complex, biological samples.

In summary, we presented a method for 3D super-resolution microscopy, which combines the high axial precision of MIET imaging with the high lateral resolution of SMLM and therefore allows for isotropic single-molecule localization in 3D. The achieved axial localization precision is below 10 nm within the first 60 nm from the gold-coated cover glass surface. By adding spacer layers or choosing a different substrate, such as graphene (*47*), the axial range and sensitivity could be adapted to a given sample. MIET-SMLM is straightforward to implement on commercial CLSMs with TCSPC capability and fast laser scanning. We have demonstrated MIET-SMLM using *d*STORM for imaging cellular structures. Moreover, dual-color MIET imaging via spectral demixing allowed for simultaneous imaging of two different biological structures without compromising the resolution. MIET-SMLM could become a powerful tool for multiplexed 3D super-resolution microscopy with exceptionally high isotropic resolution and manifold applications in structural biology.

MATERIALS AND METHODS

Confocal microscope

Fluorescence lifetime measurements were performed on a custom-built confocal setup. Fluorescence excitation was done with a 640-nm, 40-MHz pulsed diode laser (PDL 800-B driver with LDH-D-C-640 diode, PicoQuant). After passing through a cleanup filter (MaxDiode 640/8, Semrock), a quarter-wave plate converted the linearly polarized laser light into circularly polarized light. Subsequently, the laser beam was coupled into a single-mode fiber (PMC-460Si-3.0-NA012-3APC-150-P, Schäfter + Kirchhoff) with a fiber coupler (60SMS-1-4-RGBV-11-47, Schäfter + Kirchhoff). After the fiber, the output beam was collimated by an air objective (UPlanSApo 10×/0.40 NA, Olympus). An ultraflat quad-band dichroic mirror (ZT405/488/561/640rpc, Chroma) reflected the excitation light toward the microscope. After passing a laser scanning system (FLIMbee, PicoQuant), the light was sent into the custom side port of the microscope (IX73, Olympus). The three galvo mirrors of the scanning system deflect the beam while preserving the beam position in the back focal plane of the objective (UApo N 100×/1.49 NA oil, Olympus). Sample position is adjusted by using the manual *XY* stage of the microscope (IX73, Olympus) and a *z* piezo stage (Nano-ZL100, Mad City Labs). Fluorescence light was collected by the same objective and descanned by the scanning system. An achromatic lens (TTL180-A, Thorlabs) focuses the descanned beam onto a pinhole (100-µm P100S, Thorlabs). Backscattered/back-reflected excitation laser light was blocked by a long-pass filter (635 LP Edge Basic, Semrock). After the pinhole, the emission light was collimated by a 100-mm lens. An additional band-pass filter (BrightLine HC 679/41, Semrock) was used for further rejection of scattered excitation light. Last, the emission light was focused onto a single-photon avalanche diode (SPAD) detector (SPCM-AQRH, Excelitas) with an achromatic lens (AC254-030-A-ML, Thorlabs).

For sd-*d*STORM, a dichroic mirror (FF685-Di02, Semrock) was used to split the fluorescence signal into two channels, which were focused onto two separate SPAD detectors. In front of the two detectors, band-pass filters BrightLine HC 679/41 and BrightLine HC 708/75 were placed, respectively (for more details, see fig. S1).

Output signals of the photon detectors were recorded with a TCSPC electronics (HydraHarp 400, PicoQuant) that was synchronized by a trigger signal from the excitation laser. Images were acquired with the software SymPhoTime 64 (PicoQuant), which controlled both the TCSPC electronics and the scanner. Typically, samples were scanned with a virtual pixel size of 100 nm, a dwell time of 2.5 µs per pixel, and a TCSPC time resolution of 16 ps.

MIET imaging

For MIET measurements of U2OS cells, samples were prepared on glass coverslips coated with 2 nm of titanium, 10 nm of gold, 1 nm of titanium, and 5 nm of silicon dioxide. Gold layers were generated by chemical vapor deposition using an electron beam source (Univex 350, Leybold) under high-vacuum conditions (~10^{-6} mbars). A thin silicon dioxide layer of a few nanometers was used for both protecting the gold layer from the thiol buffer and achieving an optimal distance between sample and gold layer (most sensitive region of MIET curve).

For MIET calibration measurements, we used gold-coated coverslips with SiO_2 spacers of different thickness on top. The coverslips were rinsed with methanol and dried using air flow. Four-well silicone inserts (Ibidi 80469, Germany) were attached to a coverslip to form four-well chambers. DNA-fluorophore constructs were immobilized on the surface using biotin-avidin as follows: BSA-biotin (A8549, Sigma-Aldrich) was dissolved and diluted in buffer A [10 mM tris and 50 mM NaCl (pH 8.0)] to a concentration of 0.5 mg/ml and added to the chamber and incubated overnight at 4°C. Afterward, the chamber was flushed with buffer A up to the volume of the chamber at least three times. Neutravidin (31000, Thermo Fisher Scientific) was dissolved and diluted in buffer A to a concentration of 0.5 mg/ml, injected into a chamber, and incubated for 5 to 15 min. Then the neutravidin solution was removed from a chamber by rinsing with buffer A at least three times. Solution with dsDNA-fluorophore at a concentration of 500 pM was added to a chamber and incubated for a few minutes until sparse coverage of the surface with fluorescent molecules was achieved. The coverage density was controlled visually, and once a desired surface coverage density was reached, the dsDNA leftovers were washed out with B4 buffer [10 mM tris and 1 mM EDTA (pH 8.0)] including 500 mM NaCl. Imaging was done until all fluorophores photobleached.

Data analysis

Confocal *d*STORM measurements were analyzed with an extended version of the software packed TrackNTrace (*39*, *48*). From raw scan data, images were generated by combining 10 scans into one frame. When using TrackNTrace, for localization, the detection plugin cross-correlation with default parameters and the refinement plugin TNT Fitter with pixel-integrated Gaussian maximum likelihood fitting were used. Localizations in adjacent frames with a distance of less than 100 nm were connected to a "track," and the position was refitted using the sum of all images of the track.

For spectral splitting, localizations were first done on a sum image of both channels. Subsequently, the amplitudes of the Gaussian PSFs were fitted separately in both spectral channels while keeping the PSF size and position fixed.

For lifetime fitting, for each localized molecule, a TCSPC histogram was generated by collecting all photons in the corresponding frame with less than 2 σ_{PSF} distance from the molecule's center position. The TCSPC histogram was then fitted with a monoexponential decay function using a maximum likelihood estimator (*49*) to determine the lifetime.

Single-molecule lifetimes were converted into axial positions using a precalculated MIET curve. Localizations were filtered on the basis of PSF size (100 nm < σ_{PSF} < 160 nm), number of photons (>200), and quality of the lifetime fit (0.9 < Pearson's χ^2 < 1.1). For spectral splitting, molecules were sorted on the basis of the spectral intensity ratio, defined as the intensity in the long wavelength channel divided by the sum of both intensities. Molecules with a ratio below 0.5 were classified as AF 647, and molecule above 0.7 was classified as CF 680. For super-resolution image reconstruction, localizations were reconstructed with a PSF of 15 nm for the large images and 5 nm for the *xz* cross sections.

The calibration measurements (Fig. 1) were analyzed in a similar fashion to the *d*STORM cell measurements with the following differences: For localization, 100 scans were combined to one frame, and molecules not detected in at least two frames were rejected during filtering. For each spacer thickness, the molecule heights were calculated with the corresponding MIET curve. The MIET curve shown in Fig. 1C is calculated for a sample without spacer. The version of TrackNTrace used for this work includes a new plugin for spectral splitting and a data visualizer with added functionalities for MIET, and it is freely available on GitHub (https://github.com/scstein/TrackNTrace).

Modeling of MIET curves

MIET height-versus-lifetime curves were calculated using published scripts (*50*). For this purpose, the geometric structure of the sample (layer composition and thickness values), the numeric aperture of the objective, the emission maximum of the fluorophore, its fluorescence lifetime, and its fluorescence quantum yield have to be known. Quantum yield values were adjusted for the actual sample environment by multiplying measured quantum yield values with the ratio of the lifetime measured in the sample to the lifetime measured during quantum yield measurement. In all cases, a random fluorophore orientation was assumed.

Preparation of dsDNA for surface labeling

The following DNA sequences were used for surface immobilization: the single-stranded DNA (ssDNA 1) (5′→ 3′) biotin-AATCGATGATAGACGTTGTGGCTGC was biotinylated at its 5′ end, while its complementary single-stranded DNA (ssDNA 2) GCAGCCACAACGTCTATCATCGATT-fluorophore was labeled with a fluorophore (AF 647) on its 3′ end. These two DNA strands were hybridized at high concentration (200 nM) by heating up to 94°C in an annealing buffer for 5 min and then gradually cooled down to room temperature (30 min). The obtained dsDNA had a length of 25 nucleotides, which ensured its stability on a time scale of several weeks. The construct was designed in such way that the fluorophore faced the surfaces therefore decreasing the linkage errors in single-molecule localization. The extra height due to the thickness of the biotin-avidin layer is between 12 and 16 nm (*30*), and it was taken into account when estimating the total height above the gold layer.

*d*STORM buffer composition

For conventional *d*STORM imaging (using AF 647 and CF 680), a switching buffer consisting of 50 mM cysteamine in phosphate-buffered saline (PBS; pH 7.4) was used. For reductive SMLM using Cy5b, the

following procedure was used: First, the sample was incubated in 0.1% $NaBH_4$/PBS solution for 30 min. Then, it was washed two to three times with 0.1% $NaBH_4$/PBS and measured in the same 0.1% $NaBH_4$/PBS solution. After the measurement, it was washed and stored in PBS.

Cell culture and antibody labeling

Cell lines were cultured at 37°C in 5% CO_2 in T25 culture flasks (Thermo Fisher Scientific, no. 156340). U2OS (human osteosarcoma cell line) were cultivated in Dulbecco's modified Eagle's medium (F12) with L-glutamine (Sigma-Aldrich, D8062) supplemented with 10% fetal bovine serum (Sigma-Aldrich, F7524) and penicillin (100 U/ml) + streptomycin (0.1 mg/ml; Sigma-Aldrich, P4333).

For labeling antibodies with a varying degree of labeling (DOL), an excess of AF 647 *N*-hydroxysuccinimide (NHS) ester (LifeTech, A20106), CF680 NHS ester (Biotium, no. 92220), or Cy5B NHS ester, respectively, was used. The latter was synthesized by M. Schnermann (National Cancer Institute, Frederick, MD, USA) (*44*). Goat anti-rabbit immunoglobulin G (IgG) (IgG-gar; Invitrogen, 31212) and goat anti-mouse IgG (IgG-gam; Sigma-Aldrich, SAB3701063-1) were used as secondary antibodies for staining. For NHS labeling, 100 μg of antibodies was transferred to 100 mM sodium tetraborate buffer (pH 9.5) (Fluka, 71999) using Zeba Spin Desalting Columns 40 K molecular-weight cutoff (MWCO) (Thermo Fisher Scientific, no. 87766) according to the protocol suggested by the manufacturer. Different excesses of NHS ester dyes were used to achieve different DOLs. For IgG-gar coupled with AF 647, CF680, or Cy5B, an excess of 25×, 15×, and 20× was used to reach a DOL of ~8.3. 4.9, and 2.3, respectively. For IgG-gam coupled with AF 647 or CF680, an excess of 25× and 15× was used to reach a DOL of ~8.5 and ~7.7, respectively. The reaction proceeded for 4 hours at room temperature while protected from light. Labeled antibodies were separated from free dye, washed three times, and reconstituted into PBS (Sigma-Aldrich, D8537-500 ML) using Zeba Spin Desalting Columns 40-kDa MWCO. Antibody concentration and DOL were determined by ultraviolet-visible absorption spectrometry (Jasco, V-650).

Immunostaining

For immunostaining, cells were seeded onto gold-coated coverslips at a concentration of 5×10^4 cells per coverslip and cultivated overnight at 37°C and 5% CO_2. For microtubule and clathrin immunostaining, cells were washed with prewarmed (37°C) PBS and permeabilized for 2 min with 0.3% glutaraldehyde (GA) + 0.25% Triton X-100 [Electron Microscopy Sciences (EMS), 16220 and Thermo Fisher Scientific, 28314] in prewarmed (37°C) cytoskeleton buffer (CB) consisting of 10 mM MES (pH 6.1) (Sigma-Aldrich, M8250), 150 mM NaCl (Sigma-Aldrich, 55886), 5 mM EGTA (Sigma-Aldrich, 03777), 5 mM glucose (Sigma-Aldrich, G7021), and 5 mM $MgCl_2$ (Sigma-Aldrich, M9272). After permeabilization, cells were fixed with a prewarmed (37°C) solution of 2% GA in CB for 10 min. After fixation, cells were washed twice with PBS and reduced with 0.1% sodium borohydride (Sigma-Aldrich, 71320) in PBS for 7 min. Cells were again washed three times with PBS before blocking with 5% BSA (Roth, no. 3737.3) in PBS for 1 hour. Subsequently, microtubule samples were incubated with rabbit anti–α-tubulin antibody (4 ng/μl; Abcam, no. ab18251), and clathrin samples were incubated with rabbit anti-clathrin antibody (4 ng/μl; Abcam, no. ab21679) or mouse anti-clathrin antibody (Abcam, no. 2731) in blocking buffer for 1 hour. After primary antibody incubation, cells were washed thrice with 0.1% Tween 20 (Thermo Fisher Scientific, 28320) in PBS for 15 min. After washing, cells were incubated in blocking buffer with custom-labeled secondary antibodies (8 ng/μl) or commercial IgG-gam-F(ab′)2–AF 647 (DOL of ~3) (8 ng/μl; Thermo Fisher Scientific, A-21237) for 45 min. After secondary antibody incubation, cells were again washed three times with 0.1% Tween 20 in PBS for 15 min. After washing, a post-fix with 4% formaldehyde (Sigma-Aldrich, F8775) in PBS for 10 min was performed followed by three additional washing steps with PBS.

Fluorescence quantum yield measurements

We used a plasmonic nanocavity and a custom-built scanning confocal microscope for

absolute fluorescence quantum yield determination (*45*). The cavity mirrors were prepared by chemical vapor deposition of silver on the surface of a clean glass cover slide (bottom mirror) and a plane-convex lens (top mirror) by using a Leybold Univex 350 evaporation machine under high-vacuum conditions (~10^{-6} mbars). The bottom and top mirrors had a thickness of 30 and 60 nm, respectively. The distance between the cavity mirrors was monitored by measuring a white-light transmission spectrum using an Andor SR 303i spectrograph and an electron-multiplying charge-coupled device camera (Andor iXon DU897 BV). By fitting these spectra with a standard Fresnel model of transmission through a stack of plan-parallel layers, one can determine the precise cavity length (distance between mirrors). Fluorescence lifetime measurements were performed with a custom-built confocal microscope equipped with an objective lens of high NA (Apo N, 60×/1.49 NA oil immersion, Olympus). A white-light laser system (Fianium SC400-4-20) with a tunable filter (AOTFnC-400.650-TN) served as excitation source (λ_{exc} = 640 nm). Collected fluorescence was focused onto the active area of a single-photon detection module (PDM Series, Micro Photon Devices). Data acquisition was accomplished with a multichannel picosecond event timer (PicoQuant HydraHarp 400). Photon arrival times were histogrammed (bin width of 50 ps) for obtaining fluorescence decay curves. From the obtained lifetime–versus–cavity size curves, absolute values of quantum yields were obtained by fitting an appropriate model (*45*).

SUPPLEMENTARY MATERIALS

Supplementary material for this article is available at https://science.org/doi/10.1126/sciadv.abo2506

View/request a protocol for this paper from *Bio-protocol*.

REFERENCES AND NOTES

1. S. W. Hell, Far-field optical nanoscopy. *Science* **316**, 1153–1158 (2007).
2. S. W. Hell, S. Jakobs, L. Kastrup, Imaging and writing at the nanoscale with focused visible light through saturable optical transitions. *Appl. Phys. A* **77**, 859–860 (2003).
3. M. J. Rust, M. Bates, X. Zhuang, Sub-diffraction-limit imaging by stochastic optical reconstruction microscopy (STORM). *Nat. Methods* **3**, 793–795 (2006).
4. E. Betzig, G. H. Patterson, R. Sougrat, O. W. Lindwasser, S. Olenych, J. S. Bonifacino, M. W. Davidson, J. Lippincott-Schwartz, H. F. Hess, Imaging intracellular fluorescent proteins at nanometer resolution. *Science* **313**, 1642–1645 (2006).
5. A. Sharonov, R. M. Hochstrasser, Wide-field subdiffraction imaging by accumulated binding of diffusing probes. *Proc. Natl. Acad. Sci. U.S.A.* **103**, 18911–18916 (2006).
6. J. Schnitzbauer, M. T. Strauss, T. Schlichthaerle, F. Schueder, R. Jungmann, Super-resolution microscopy with DNA-PAINT. *Nat. Protoc.* **12**, 1198–1228 (2017).
7. M. Heilemann, S. van de Linde, M. Schüttpelz, R. Kasper, B. Seefeldt, A. Mukherjee, P. Tinnefeld, M. Sauer, Subdiffraction-resolution fluorescence imaging with conventional fluorescent probes. *Angew. Chem. Int. Ed.* **47**, 6172–6176 (2008).
8. M. Dyba, S. W. Hell, Focal spots of size λ/23 open up far-field florescence microscopy at 33 nm axial resolution. *Phys. Rev. Lett.* **88**, 163901 (2002).

9. M. F. Juette, T. J. Gould, M. D. Lessard, M. J. Mlodzianoski, B. S. Nagpure, B. T. Bennett, S. T. Hess, J. Bewersdorf, Three-dimensional sub–100 nm resolution fluorescence microscopy of thick samples. *Nat. Methods* **5**, 527–529 (2008).
10. B. Huang, W. Wang, M. Bates, X. Zhuang, Three-dimensional super-resolution imaging by stochastic optical reconstruction microscopy. *Science* **319**, 810–813 (2008).
11. S. R. P. Pavani, M. A. Thompson, J. S. Biteen, S. J. Lord, N. Liu, R. J. Twieg, R. Piestun, W. E. Moerner, Three-dimensional, single-molecule fluorescence imaging beyond the diffraction limit by using a double-helix point spread function. *Proc. Natl. Acad. Sci. U.S.A.* **106**, 2995–2999 (2009).
12. M. D. Lew, S. F. Lee, M. Badieirostami, W. E. Moerner, Corkscrew point spread function for far-field three-dimensional nanoscale localization of pointlike objects. *Opt. Lett.* **36**, 202–204 (2011).
13. Y. Shechtman, L. E. Weiss, A. S. Backer, S. J. Sahl, W. E. Moerner, Precise three-dimensional scan-free multiple-particle tracking over large axial ranges with tetrapod point spread functions. *Nano Lett.* **15**, 4194–4199 (2015).
14. P. Bon, J. Linarès-Loyez, M. Feyeux, K. Alessandri, B. Lounis, P. Nassoy, L. Cognet, Self-interference 3D super-resolution microscopy for deep tissue investigations. *Nat. Methods* **15**, 449–454 (2018).
15. M. Sauer, M. Heilemann, Single-molecule localization microscopy in eukaryotes. *Chem. Rev.* **117**, 7478–7509 (2017).
16. G. Shtengel, J. A. Galbraith, C. G. Galbraith, J. Lippincott-Schwartz, J. M. Gillette, S. Manley, R. Sougrat, C. M. Waterman, P. Kanchanawong, M. W. Davidson, R. D. Fetter, H. F. Hess, Interferometric fluorescent super-resolution microscopy resolves 3D cellular ultrastructure. *Proc. Natl. Acad. Sci. U.S.A.* **106**, 3125–3130 (2009).
17. R. Schmidt, C. A. Wurm, A. Punge, A. Egner, S. Jakobs, S. W. Hell, Mitochondrial cristae revealed with focused light. *Nano Lett.* **9**, 2508–2510 (2009).
18. F. Huang, G. Sirinakis, E. S. Allgeyer, L. K. Schroeder, W. C. Duim, E. B. Kromann, T. Phan, F. E. Rivera-Molina, J. R. Myers, I. Irnov, M. Lessard, Y. Zhang, M. A. Handel, C. Jacobs-Wagner, C. P. Lusk, J. E. Rothman, D. Toomre, M. J. Booth, J. Bewersdorf, Ultra-high resolution 3D imaging of whole cells. *Cell* **166**, 1028–1040 (2016).
19. F. Balzarotti, Y. Eilers, K. C. Gwosch, A. H. Gynnå, V. Westphal, F. D. Stefani, J. Elf, S. W. Hell, Nanometer resolution imaging and tracking of fluorescent molecules with minimal photon fluxes. *Science* **355**, 606–612 (2017).
20. K. C. Gwosch, J. K. Pape, F. Balzarotti, P. Hoess, J. Ellenberg, J. Ries, S. W. Hell, MINFLUX nanoscopy delivers 3D multicolor nanometer resolution in cells. *Nat. Methods* **17**, 217–224 (2020).
21. L. A. Masullo, F. Steiner, J. Zähringer, L. F. Lopez, J. Bohlen, L. Richter, F. Cole, P. Tinnefeld, F. D. Stefani, Pulsed interleaved MINFLUX. *Nano Lett.* **21**, 840–846 (2021).
22. M. Cardoso Dos Santos, R. Déturche, C. Vézy, R. Jaffiol, Topography of cells revealed by variable-angle total internal reflection fluorescence microscopy. *Biophys. J.* **111**, 1316–1327 (2016).
23. L. Velas, M. Brameshuber, J. B. Huppa, E. Kurz, M. L. Dustin, P. Zelger, A. Jesacher, G. J. Schütz, Three-dimensional single molecule localization microscopy reveals the topography of the immunological synapse at isotropic precision below 15 nm. *Nano Lett.* **21**, 9247–9255 (2021).
24. C. M. Winterflood, T. Ruckstuhl, D. Verdes, S. Seeger, Nanometer axial resolution by three-dimensional supercritical angle fluorescence microscopy. *Phys. Rev. Lett.* **105**, 108103 (2010).
25. J. Deschamps, M. Mund, J. Ries, 3D superresolution microscopy by supercritical angle detection. *Opt. Express* **22**, 29081–29091 (2014).
26. N. Bourg, C. Mayet, G. Dupuis, T. Barroca, P. Bon, S. Lécart, E. Fort, S. Lévêque-Fort, Direct optical nanoscopy with axially localized detection. *Nat. Photonics* **9**, 587–593 (2015).
27. A. I. Chizhik, J. Rother, I. Gregor, A. Janshoff, J. Enderlein, Metal-induced energy transfer for live cell nanoscopy. *Nat. Photonics* **8**, 124–127 (2014).
28. N. Karedla, A. I. Chizhik, I. Gregor, A. M. Chizhik, O. Schulz, J. Enderlein, Single-molecule metal-induced energy transfer (smMIET): Resolving nanometer distances at the single-molecule level. *Chem. Phys. Chem.* **15**, 705–711 (2014).
29. N. Oleksiievets, J. C. Thiele, A. Weber, I. Gregor, O. Nevskyi, S. Isbaner, R. Tsukanov, J. Enderlein, Wide-field fluorescence lifetime imaging of single molecules. *J. Phys. Chem. A* **124**, 3494–3500 (2020).
30. S. Isbaner, N. Karedla, I. Kaminska, D. Ruhlandt, M. Raab, J. Bohlen, A. Chizhik, I. Gregor, P. Tinnefeld, J. Enderlein, R. Tsukanov, Axial colocalization of single molecules with nanometer accuracy using metal-induced energy transfer. *Nano Lett.* **18**, 2616–2622 (2018).
31. H. S. Heil, B. Schreiber, R. Götz, M. Emmerling, M.-C. Dabauvalle, G. Krohne, S. Höfling, M. Kamp, M. Sauer, K. G. Heinze, Sharpening emitter localization in front of a tuned mirror. *Light Sci. Appl.* **7**, 99 (2018).
32. A. Zelená, S. Isbaner, D. Ruhlandt, A. Chizhik, C. Cassini, A. S. Klymchenko, J. Enderlein, A. Chizhik, S. Köster, Time-resolved MIET measurements of blood platelet spreading and adhesion. *Nanoscale* **12**, 21306–21315 (2020).
33. T. Baronsky, D. Ruhlandt, B. R. Brückner, J. Schäfer, N. Karedla, S. Isbaner, D. Hähnel, I. Gregor, J. Enderlein, A. Janshoff, A. I. Chizhik, Cell-substrate dynamics of the epithelial-to-mesenchymal transition. *Nano Lett.* **17**, 3320–3326 (2017).
34. A. M. Chizhik, D. Ruhlandt, J. Pfaff, N. Karedla, A. I. Chizhik, I. Gregor, R. H. Kehlenbach, J. Enderlein, Three-dimensional reconstruction of nuclear envelope architecture using dual-color metal-induced energy transfer imaging. *ACS Nano* **11**, 11839–11846 (2017).
35. R. J. Moerland, J. P. Hoogenboom, Subnanometer-accuracy optical distance ruler based on fluorescence quenching by transparent conductors. *Optica* **3**, 112–117 (2016).
36. A. Ghosh, A. I. Chizhik, N. Karedla, J. Enderlein, Graphene- and metal-induced energy transfer for single-molecule imaging and live-cell nanoscopy with (sub)-nanometer axial resolution. *Nat. Protoc.* **16**, 3695–3715 (2021).
37. A. Ghosh, A. Sharma, A. I. Chizhik, S. Isbaner, D. Ruhlandt, R. Tsukanov, I. Gregor, N. Karedla, J. Enderlein, Graphene-based metal-induced energy transfer for sub-nanometre optical localization. *Nat. Photonics* **13**, 860–865 (2019).
38. I. Kaminska, J. Bohlen, S. Rocchetti, F. Selbach, G. P. Acuna, P. Tinnefeld, Distance dependence of single-molecule energy transfer to graphene measured with DNA origami nanopositioners. *Nano Lett.* **19**, 4257–4262 (2019).
39. J. C. Thiele, D. A. Helmerich, N. Oleksiievets, R. Tsukanov, E. Butkevich, M. Sauer, O. Nevskyi, J. Enderlein, Confocal fluorescence-lifetime single-molecule localization microscopy. *ACS Nano* **14**, 14190–14200 (2020).
40. Z. Zhang, S. J. Kenny, M. Hauser, W. Li, K. Xu, Ultrahigh-throughput single-molecule spectroscopy and spectrally resolved super-resolution microscopy. *Nat. Methods* **12**, 935–938 (2015).
41. K. Spaeth, A. Brecht, G. Gauglitz, Studies on the biotin-avidin multilayer adsorption by spectroscopic ellipsometry. *J. Colloid Interface Sci.* **196**, 128–135 (1997).
42. K. I. Mortensen, L. S. Churchman, J. A. Spudich, H. Flyvbjerg, Optimized localization analysis for single-molecule tracking and super-resolution microscopy. *Nat. Methods* **7**, 377–381 (2010).
43. B. Rieger, S. Stallinga, The lateral and axial localization uncertainty in super-resolution light microscopy. *Chem. Phys. Chem.* **15**, 664–670 (2014).
44. P. Eiring, R. McLaughlin, S. S. Matikonda, Z. Han, L. Grabenhorst, D. A. Helmerich, M. Meub, G. Beliu, M. Luciano, V. Bandi, N. Zijlstra, Z.-D. Shi, S. G. Tarasov, R. Swenson, P. Tinnefeld, V. Glembockyte, T. Cordes, M. Sauer, M. J. Schnermann, Targetable conformationally restricted cyanines enable photon-count-limited applications. *Angew. Chem. Int. Ed.* **60**, 26685–26693 (2021).
45. A. I. Chizhik, I. Gregor, B. Ernst, J. Enderlein, Nanocavity-based determination of absolute values of photoluminescence quantum yields. *Chem. Phys. Chem.* **14**, 505–513 (2013).
46. S. M. Früh, U. Matti, P. R. Spycher, M. Rubini, S. Lickert, T. Schlichthaerle, R. Jungmann, V. Vogel, J. Ries, I. Schoen, Site-specifically-labeled antibodies for super-resolution microscopy reveal in situ linkage errors. *ACS Nano* **15**, 12161–12170 (2021).
47. I. Kamińska, J. Bohlen, R. Yaadav, P. Schüler, M. Raab, T. Schröder, J. Zähringer, K. Zielonka, S. Krause, P. Tinnefeld, Graphene energy transfer for single-molecule biophysics, biosensing, and super-resolution microscopy. *Adv. Mater.* **33**, 2101099 (2021).
48. S. Stein, J. Thiart, TrackNTrace: A simple and extendable open-source framework for developing single-molecule localization and tracking algorithms. *Sci. Rep.* **6**, 37947 (2016).
49. J. C. Thiele, O. Nevskyi, D. A. Helmerich, M. Sauer, J. Enderlein, Advanced data analysis for fluorescence-lifetime single-molecule localization microscopy. *Front. Bioinform.* **1**, 740281 (2021).
50. N. Karedla, A. M. Chizhik, S. C. Stein, D. Ruhlandt, I. Gregor, A. I. Chizhik, J. Enderlein, Three-dimensional single-molecule localization with nanometer accuracy using metal-induced energy transfer (MIET) imaging. *J. Chem. Phys.* **148**, 204201 (2018).

Acknowledgments: We thank I. Gregor for fruitful discussions. **Funding:** J.E., J.C.T., and O.N. are grateful to the European Research Council (ERC) via project "smMIET" (grant agreement no. 884488) under the European Union's Horizon 2020 research and innovation program. J.E. is grateful for financial support through Germany's Excellence Strategy–EXC 2067/1-390729940. M.J. and M.S. acknowledge financial support by the DFG (GRK 2157). M.S. is grateful for financial support by the European Research Council via the ERC Synergy Grant project "ULTRARESOLUTION" (project no. 951275). M.J.S. was supported by the Intramural Research Program of the National Institutes of Health, National Cancer Institute, Center for Cancer Research (BC011506). We acknowledge support by the Open Access Publication Funds of the Göttingen University. **Author contributions:** J.C.T., M.J., D.A.H., M.S., J.E., and O.N. designed the experiments. J.C.T. and O.N. generated and processed the data. D.A.H. and M.J. labeled antibodies and prepared cells for *d*STORM measurements. R.T. prepared dsDNA for surface labeling. A.C. prepared coverslips for MIET imaging. A.I.C. performed quantum yield measurements. M.J.S. performed synthesis of Cy5b dye. J.C.T. wrote the analysis software. J.C.T., M.J., D.A.H., R.T., M.S., J.E., and O.N. wrote and finalized the manuscript. **Competing interests:** A patent describing the compound used here has been submitted. The authors declare that they have no other competing interests. **Data and materials availability:** All data needed to evaluate the conclusions in the paper are present in the paper and/or the Supplementary Materials. The raw data for the MIET-SMLM measurements and a permanent copy of TrackNTrace are available at https://doi.org/10.25625/2HOMI3.

Submitted 22 January 2022
Accepted 25 April 2022
Published 8 June 2022
10.1126/sciadv.abo2506

ScienceAdvances

Isotropic three-dimensional dual-color super-resolution microscopy with metal-induced energy transfer

Jan Christoph ThieleMarvin JungblutDominic A. HelmerichRoman TsukanovAnna ChizhikAlexey I. ChizhikMartin J. SchnermannMarkus SauerOleksii NevskyiJörg Enderlein

Sci. Adv., 8 (23), eabo2506. • DOI: 10.1126/sciadv.abo2506

Science Advances (ISSN) is published by the American Association for the Advancement of Science. 1200 New York Avenue NW, Washington, DC 20005. The title *Science Advances* is a registered trademark of AAAS.